Ambient Noise Imaging of Western Europe From Combining Linear SOLA Backus–Gilbert Inference and Non-Linear Probabilistic Approaches

Ahmed Nouibat[1] [iD], **Christophe Zaroli[1], and Sophie Lambotte[1]** [iD]

[1]Université de Strasbourg, CNRS, ITES, UMR 7063, Strasbourg, France

Abstract We present a new method for ambient noise tomography, which provides robust velocity images accompanied with meaningful estimates of local resolution and uncertainty. We use the Subtractive Optimally Localized Averages (SOLA) Backus–Gilbert inference method to determine surface wave velocities as local (unbiased) averages of the "true" model parameters. Regularization on the model itself is not needed, but a compromise is sought between the local resolution and uncertainty. Then, we construct a 2D grid which efficiently accommodates the lateral variations on resolution at period. Based on this grid, we perform a probabilistic inversion to estimate V_s at depth, efficiently propagating the frequency-dependent uncertainties. Finally, we demonstrate the effectiveness of this method by deriving a robust 3D V_s model of Western Europe, using 13 years of continuous noise recordings.

Plain Language Summary Relevant physical interpretations of structural features revealed by tomographic models require information on their resolutions and uncertainties. We address this inference-oriented problem in the context of ambient noise tomography (ANT), by far the most widely used passive imaging method for investigating the 3D structure of the Earth's crust. We present a new inversion procedure, combining linear Backus–Gilbert inference and non-linear probabilistic approaches, that can infer robust velocity estimates accompanied with their local resolutions and uncertainties. This novel method paves the way for a new generation of self-consistent ANT models that can be exploited quantitatively in geological and geophysical studies.

1. Introduction

Earth's interior imaging based on seismic ambient noise has evolved rapidly over the last few decades, stimulated by increasingly dense broadband networks (e.g., USArray, AlpArray). Following the pioneering work of Shapiro et al. (2005), ambient noise tomography (ANT) has been widely applied at regional scales, demonstrating its effectiveness in imaging crustal shear velocity structures (e.g., Bensen et al., 2009; Moschetti et al., 2010; Stehly et al., 2009; Sun et al., 2010; Zheng et al., 2011). In conventional ANT, pseudo-3D V_s models are constructed in two steps: (a) 2D traveltime inversion based on ray theory, to derive frequency-dependent surface wave velocity maps, (b) 1D inversion of local dispersion curves to derive V_s at depth, assuming a laterally homogeneous subsurface. Despite its simplifying assumptions, ANT remains a first choice for dealing with large databases, although alternative techniques, more computationally demanding, such as adjoint ANT (AANT) have recently proved their efficiency in regional-scale applications (e.g., Chen et al., 2014; Liu et al., 2017; Wang et al., 2018).

Regardless the broad scope of ANT, quantitative assessment of resolution and uncertainty of the relevant models has often been ignored or poorly addressed—yet crucial for constraining the physical and geological interpretations. Indeed, the classical methods used to solve the 2D inverse problem of ANT are not inherently designed to infer the local resolution and uncertainty at period, which makes it difficult to propagate a realistic constraint on their variability into the V_s structure at depth. Most linear approaches remove the inherent non-uniqueness of the solution by adding ad hoc regularization (e.g., Boschi & Dziewonski, 1999; Kennett et al., 1988; Rawlinson & Sambridge, 2003). The values of latter's parameters are usually chosen on the basis of subjective arguments, that is to find a compromise between model complexity and data misfit. This choice inevitably biases the model estimates—the solution can be locally biased toward lower or higher amplitudes in regions of poor and/or anisotropic seismic coverage (Zaroli et al., 2017). Such regularization also implies renouncing the propagation of data noise into the model, which could statistically bias the estimate of uncertainty. Statistical techniques (e.g., jackknife, bootstrap) used to evaluate uncertainty often overestimate or underestimate

its magnitude as the model complexity varies with the level of regularization (Rawlinson et al., 2014). Bayesian strategies, however, tackle the solution non-uniqueness through ensemble inference over the model parameters space (e.g., Bodin & Sambridge, 2009; Bodin et al., 2012; Galetti et al., 2017). This enables the data noise propagation, while the model uncertainty is usually represented by the variance map of the solution ensemble. Nevertheless, to reduce the dimensionality of the problem, data noise (treated as unknown) is often parametrized with the standard deviation of a single Gaussian distribution describing errors in the data, or by means of some hyperparameters governing distance-dependent parametrizations. Thus, a wrong choice of the distribution prior or proposal variance for these hyperparameters could bias the posterior model ensemble.

In linear approaches, calculating the full generalized inverse—which is computationally challenging in most large-scale tomographic applications—is needed to infer both model resolution and covariance matrices (e.g., Nolet, 2008; Zaroli et al., 2017). Hence the resolution matrix is often not determined or only approximated (e.g., Rawlinson & Spakman, 2016; Trampert et al., 2013). As a result, assessment of resolution has often been reduced to checker-board or discrete spikes sensitivity tests, which suffer from a number of drawbacks (e.g., Lévêque et al., 1993; Rawlinson & Spakman, 2016). The absence of accurate resolution analysis in the 2D inversion step results in arbitrary choices of the depth inversion grid—which controls the lateral smoothness of the V_s images, a proxy for the lateral resolution. In most applications, spacing and spatial distribution of this grid nodes are chosen to fit the computing resources, and do not reflect the actual local resolution. For the sake of clarity, here we do not refer to the vertical resolution, since it is not affected by the grid choice, but rather by the sensitivity of inverted data in the considered period range (e.g., Lin et al., 2008).

Backus–Gilbert (B–G) linear inversion deals in depth with the appraisal problem through a trade-off between model resolution and variance (uncertainty), with no ad hoc constraints on the model itself (Backus & Gilbert, 1967, 1968). In this paradigm, the solution non-uniqueness is broken by evaluating spatially localized, weighted averages of the "true" model parameters, which makes possible to infer all at once the model estimates and the underlying resolution and uncertainty. Zaroli (2016) proposed a computationally efficient variant of the B–G inversion (the discrete SOLA–BG), and demonstrated its robustness in providing robust tomographic images with meaningful estimates of resolution and uncertainty, in the scope of global-scale tomography. In this approach, the averaging kernels are explicitly constructed based on a priori informations about the local resolution, represented by *SOLA target kernels*. The choices of their size/form, as well as the SOLA trade-off parameter do not introduce averaging bias on the model parameters estimate, contrary to regularization constraints in the traditional tomographic methods (Zaroli et al., 2017).

In this study, we present an ANT strategy based on 2D SOLA–BG and 1D probabilistic inversions, which yields velocity models and their appraisals. Exploiting the inherent strength of each technique, we derive unbiased surface wave velocity maps, and robust 1D V_s models effectively constrained by meaningful quantitative estimates of local resolution and uncertainty at period. Additionally, we propose an efficient approach to build meaningful depth-inversion grids based on the resolution estimates. We demonstrate the effectiveness of this method through a real data application on the scale of Western Europe. In the light of this application, we will document key points related to the choice of SOLA–BG tunable parameters and the underlying effects, as well as uncertainty propagation at depth.

2. Method

2.1. SOLA–BG Inversion for Surface Wave Velocities

We derive group/phase velocity maps by performing a 2D traveltime tomography based on SOLA–BG linear inversion (Zaroli, 2016; Zaroli et al., 2017). The model parameters are velocity perturbations $\boldsymbol{m} = (\delta U_k)_{1 \leq k \leq M}$ with respect to a 2D homogeneous velocity model, and data correspond to traveltime perturbations $\boldsymbol{d} = (\delta t_i)_{1 \leq i \leq N}$. Here, the physical model space is discretized into M 2D cells based on a spherical parametrization grid. The linear forward problem has the form $\boldsymbol{d} = \boldsymbol{Gm} + \boldsymbol{n}$, where $\boldsymbol{G}$ denotes the sensitivity matrix, $\boldsymbol{m}$ the "true" model parameters and $\boldsymbol{n}$ the data noise. We assume uncorrelated data errors, having normal distributions with zero mean $n_i = \mathcal{N}(0, \sigma_{d_i}^2)$. We seek to estimate weighted local averages over the "true" model: $\widehat{\delta U}_k = \hat{\boldsymbol{R}}_k \boldsymbol{m} + \mathcal{N}(0, \sigma_{\hat{m}_k}^2)$, where $\hat{\boldsymbol{R}}_k$ is the kth row of the resolution matrix (i.e., $\hat{\boldsymbol{R}} = \hat{\boldsymbol{G}}^\dagger \boldsymbol{G}$) referred to as *resolving kernel*, and $\sigma_{\hat{m}_k}$ the standard deviation of a normal distribution that describes the model uncertainty. The

kth velocity perturbation is directly inferred from the kth row of the generalized inverse $\hat{\boldsymbol{G}}_k^{\dagger} = \left(\hat{G}_{ki}^{\dagger}\right)_{1 \leq i \leq N}$, as linear combination of data: $\widehat{\delta U}_k = \hat{\boldsymbol{G}}_k^{\dagger} \boldsymbol{d}$. To achieve this, each row $\hat{\boldsymbol{G}}_k^{\dagger}$ is obtained by solving the minimization problem

$$\min_{\hat{\boldsymbol{G}}_k^{\dagger}} \sum_j \mathbb{S}_j \left(A_j^{(k)} - T_j^{(k)}\right)^2 + \eta_k^2\, \sigma_{\hat{m}_k}^2, \quad \text{s.t.} \sum_j \mathbb{S}_j A_j^{(k)} = 1. \tag{1}$$

where the first term represents a resolution misfit and the second the model variance. $\boldsymbol{A}^{(k)}$ denotes the averaging kernel of the kth cell, as defined by $A_j^{(k)} = \hat{R}_{kj}/\mathbb{S}_j$ at the jth cell of area $\mathbb{S}_j$. The *target resolving kernel*, $\boldsymbol{T}^{(k)}$, represents the desired local resolution. Hence, we minimize a resolution misfit rather than a data misfit, without any regularization applied directly to the model $\hat{\boldsymbol{m}}$ itself. Constraint in Equation 1 ensures that no averaging bias is introduced (Nolet, 2008; Zaroli et al., 2017). Here, the value η_k controls the propagation of data noise into the local average estimate, and therefore the trade-off resolution versus uncertainty. An optimal compromise is to choose η_k near to the maximum curvature of the trade-off L-curve. The form and size of $\boldsymbol{T}^{(k)}$ is an a priori of the inverse problem. Target kernels are chosen to be circular with a radius representing the target local resolution.

We solve the problem (Equation 1) using the LSQR-based (Paige & Saunders, 1982) approach proposed by Zaroli (2016). The generalized inverse coefficients obtained are then used to infer velocities, their resolution $\boldsymbol{A}^{(k)}$ and uncertainty $\sigma_{\hat{m}_k}$. $\boldsymbol{A}^{(k)}$ and $\sigma_{\hat{m}_k}$ are estimated locally by the linear relations: $\sigma_{\hat{m}_k}^2 = \sum_i \left(x_i^{(k)} \sigma_{d_i}\right)^2$ and $A_j^{(k)} = \frac{1}{\mathbb{S}_j} \sum_i x_i^{(k)} G_{ij}$, with $\left(x_i^{(k)}\right)_{1 \leq i \leq N}$ the N coefficients of $\hat{\boldsymbol{G}}_k^{\dagger}$.

2.2. Resolution-Based Depth Inversion Grid

Our aim at this stage is to construct a 2D grid of nodal points that adapts to the variability of local resolution at period, and use it to extract dispersion curves and their uncertainties for the depth inversion. However, the process of extracting dispersion curves is meaningful if the sampled maps display similar local resolutions, that is, spatially localized averaging kernels that are similar for all the considered periods. To achieve this, we use the same grid and target kernels in the SOLA–BG inversion for all periods.

Instead of using the distribution of SOLA–BG nodes for depth inversion, which requires rather costly computations, we space the nodes at a distance relative to the targeted local resolution at period, so that the dispersion curves are only extracted at relevant locations as regards the actual resolution. To achieve this, we follow the strategy of Nolet and Montelli (2005) and Zaroli (2010), which consists of iteratively adjusting the spatial locations of the nodes to minimize the total energy function

$$E = \sum_{j=1}^{M} \sum_{k \in N_j} \frac{(L_{jk} - l_{jk})^2}{l_{jk}^2} \tag{2}$$

where L_{jk} is the distance between nodes j and k in a Delaunay mesh of spherical triangles, l_{jk} is the average a priori resolving length given as function of the average local resolution (r_{jk}) between the two nodes $(l_{jk} = \alpha\, r_{jk}, \alpha \leq 1)$, N_j are the neighbors of node j and M is the total number of nodes. We solve this non-linear optimization problem using the conjugate gradient method. We construct the starting grid by iteratively subdividing triangles until their side's length is close to the desired node spacing imposed by the local resolving length.

2.3. Probabilistic Inversion for Shear Wave Velocities

At each node of the obtained 2D grid, we derive a 1D V_s model at depth, based on the SOLA–BG local dispersion curve and the underlying uncertainties. We design a probabilistic inversion procedure consisting of two steps: (a) library-based inversion, (b) McMC Bayesian inversion. The first aims to construct a first-order velocity model with marked interfaces representing the main geological discontinuities (e.g., basement, Moho). We perform a grid search over a set of five-layers synthetic models, parametrized by thickness, and isotropic $\{V_p, V_s, \rho\}$. For simplicity, we assume uncorrelated data uncertainties and covariance matrix $\boldsymbol{C}_d$ that

follows a multivariate normal distribution with zero mean. The reduced chi-square misfit function $\chi_{red}^2(\boldsymbol{m},\boldsymbol{d},\boldsymbol{\sigma}_d) = \frac{1}{N}(g(\boldsymbol{m}) - \boldsymbol{d})^T C_d^{-1}(g(\boldsymbol{m}) - \boldsymbol{d})$ is used to evaluate discrepancies between observed dispersion curve $\boldsymbol{d} = (\hat{U}_i)_{1 \leq i \leq N}$ and synthetics $g(\boldsymbol{m})$, given the uncertainties $\boldsymbol{\sigma}_d = (\sigma_{\hat{U}_i})_{1 \leq i \leq N}$ on $\boldsymbol{d}$. We obtain a deterministic solution by weighting the models by their $1/\chi_{red}^2$ values, and calculating the ensemble average.

To better account for structural complexity and improve the data fit, this solution is used as a reference model in a Bayesian inversion, more efficient in exploring the multi-dimensional model parameters space. The posterior distribution $p(\boldsymbol{m}|\boldsymbol{d})$ of a model $\boldsymbol{m}$ is given by the Bayes's theorem: $p(\boldsymbol{m}|\boldsymbol{d}) \propto p(\boldsymbol{d}|\boldsymbol{m})p(\boldsymbol{m})$, where $p(\boldsymbol{d}|\boldsymbol{m})$ is the likelihood and $p(\boldsymbol{m})$ the prior. We evaluate the likelihood using the Gaussian function

$$p(\boldsymbol{d}|\boldsymbol{m}) = \frac{1}{\prod_{i=1}^N \left(\sqrt{2\pi}\,\sigma_{\hat{U}_i}\right)}\exp\left(-\frac{1}{2}\sum_{i=1}^N \left[\frac{g(\boldsymbol{m})_i - \hat{U}_i}{\sigma_{\hat{U}_i}}\right]^2\right) \qquad (3)$$

where $\sigma_{\hat{U}_i}$ is the velocity uncertainty for the *ith* period, $\hat{U}_i$ and $g(\boldsymbol{m})_i$ are the *ith* values in the observed and synthetic dispersion curves, respectively. We parametrize each layer by perturbations on V_s and V_p/V_s with respect to the reference model, and sample the posterior distributions using a McMC algorithm. This approach is similar to the one described in Yuan and Bodin (2018), except that we do not consider the data uncertainties as unknowns, nor as represented by a single hyper-parameter. At each iteration, a new model $\boldsymbol{m}'$ is proposed according to Gaussian distributions centered on the parameter value in the current model $\boldsymbol{m}$. The model perturbation is chosen randomly from the following: (a) modify a layer depth, (b–c) perturb V_s or V_p/V_s in one layer, (d) add new layer, (e) remove an existing layer. The model proposal is then accepted or rejected with a probability proportional to the ratio of likelihood functions of $\boldsymbol{m}$ and $\boldsymbol{m}'$. We refer the reader to Bodin et al. (2012) and Yuan and Bodin (2018) for more details about the computation of acceptance probability.

We exploit the Delaunay triangulation of the optimal set of nodes to interpolate V_s at the locations of the other grid nodes. To achieve this, we perform a linear interpolation based on barycentric coordinates, at each depth. We locate the three vertices $\boldsymbol{p}_i (i = 1,2,3)$ of the spherical triangle enclosing each node, and estimate $V_s(\boldsymbol{r}, z)$ at the node location $\boldsymbol{r}$ by linearly interpolating the vertices values, using the normalized barycentric coordinates $b_i (i = 1,2,3)$: $V_s(\boldsymbol{r},z) = \sum_{i=1}^3 b_i V_s(\boldsymbol{p}_i, z)$. Hence, this interpolation, which can be seen as a weighted average, is more convenient than classical interpolations. Model uncertainties (posterior ensemble variances) are interpolated using the same procedure.

3. Application: Imaging of the European Lithosphere

Following the deployment of the AlpArray seismic network (AASN; Hetényi et al., 2018), Western Europe has become one of the most densely instrumented regions, providing an ideal setting for 3D imaging of the crust and upper mantle based on ambient noise. Thus, several ANT were conducted at continental and regional scales (e.g., Kvapil et al., 2021; Lu et al., 2018; Nouibat, Stehly, Paul, Schwartz, Bodin, et al., 2022; Sadeghi-Bagherabadi et al., 2021; Schippkus et al., 2018). ANT models covering the western Mediterranean region have substantially improved the knowledge of the 3D structure beneath the Alps-Apennines-Ligurian complex system, providing new insights for geological and geodynamic modeling (Paul et al., 2024). However, none of them provide constraints on the local resolution and uncertainty. Applying the method described in Section 2, we aim to address this issue by constructing the first 3D V_s model accompanied by robust quantitative appraisals.

3.1. Data Set

We built a comprehensive data set of Rayleigh wave group velocity measurements from vertical component noise correlations of 3,000 broadband stations available between 2010 and 2023 (Figure 1a). To date, this is the largest noise database in the region, with almost 5 million correlations. Daily records are processed following the procedure described in Nouibat, Stehly, Paul, Schwartz, Bodin, et al. (2022) and Nouibat, Stehly, Paul, Schwartz, Rolland, et al. (2022). Group velocity dispersion curves are measured using multiple filter analysis (MFA, Dziewonski et al., 1969; Herrmann, 1973) at periods in the range 5–80 s. Similarly to Nouibat, Stehly, Paul, Schwartz, Bodin, et al. (2022), we keep only reliable measurements based on SNR and inter-station distance criteria (2% to 30% selected measurements depending on the period).
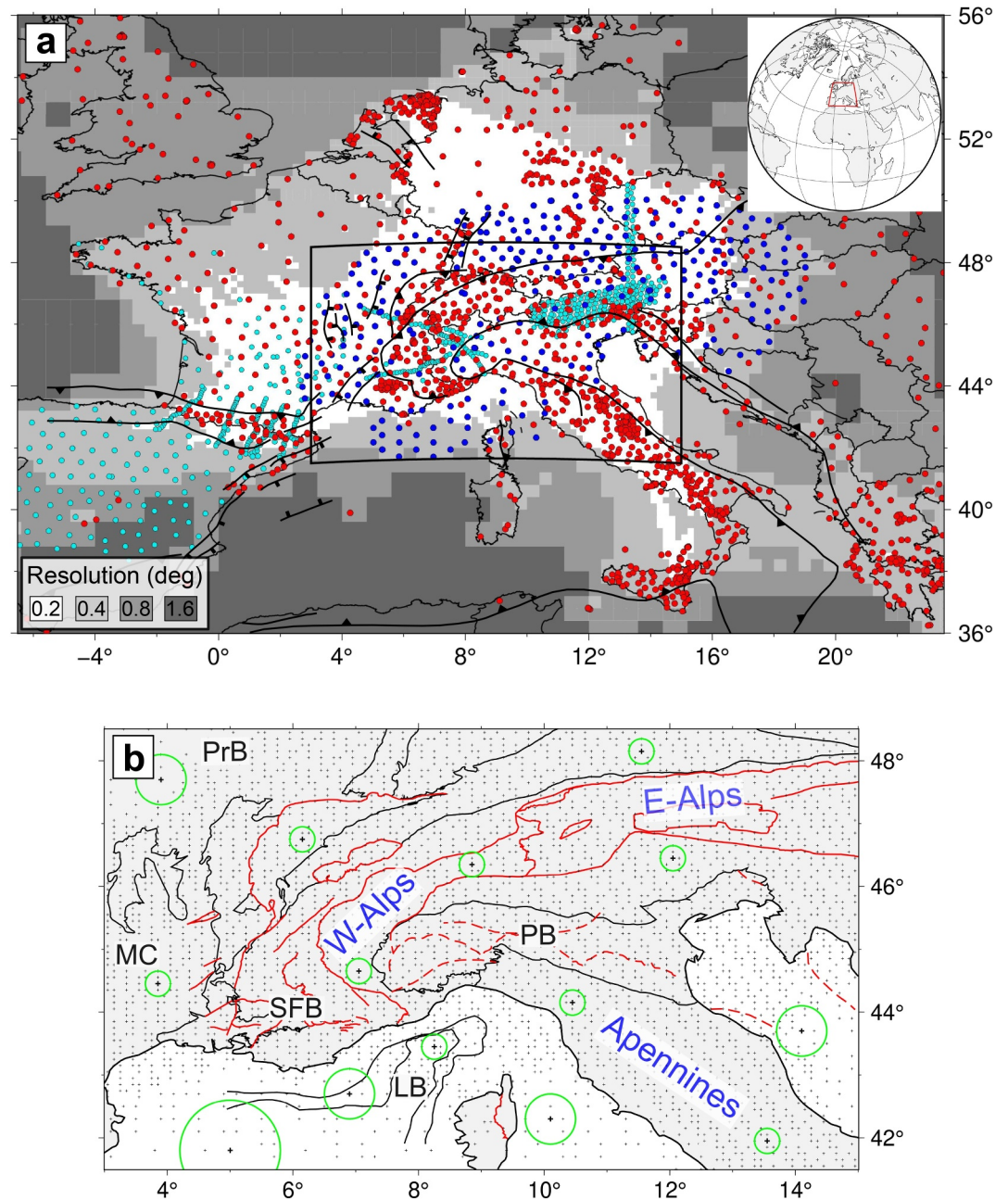
Figure 1. (a) Target resolution map with locations of seismic stations used in this study (red circles: permanent networks, blue: AlpArray network, cyan: other temporary networks). The thick black lines show the main geological boundaries (modified from Faccenna et al., 2014). (b) Zoom on the Alpine region showing the grid nodes of the depth inversion. Thick black and red lines show the main geologic units, modified from Handy et al. (2010) and Rollet et al. (2002). Green circles: shapes of some SOLA target resolving kernels.

We assume that the uncertainty in the traveltime measurement at a given period is 10% of the calculated traveltime in a homogeneous 2D model given by the average of velocity measurements. We have chosen to be cautious regarding the uncertainty magnitude, given that it is rather complicated in practice to be assessed precisely for noise data, and the resulting model uncertainties fall well within the typical range of 0.01–0.1 km/s. Furthermore, it makes sense to assign higher uncertainties to longer paths, as they integrate more velocity structures, hence, more structural complexity, being likely to accumulate a higher level of uncertainty. Finally, by overestimating
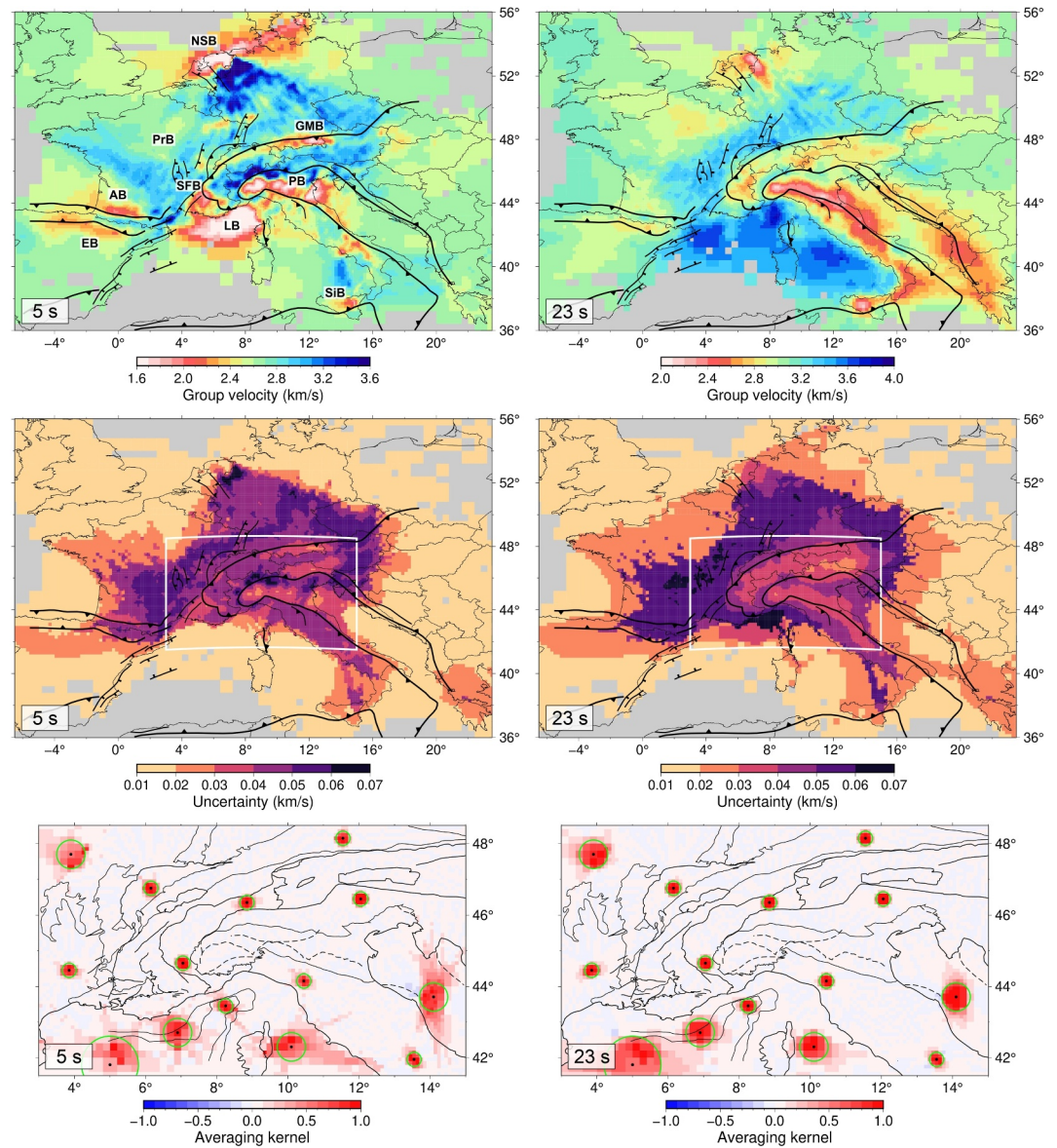
Figure 2. Group velocity maps with their uncertainty and resolution estimates. Acronyms in the 5-s velocity map refer to Po basin (PB), Ligurian basin (LB), Southeast-France basin (SFB), Sicily fold-and-thrust belt (SiB), German Molass basin (GMB), Parisian basin (PrB), North-Sea basin (NSB), Aquitaine basin (AB) and Ebro basin (EB). The SOLA resolving kernels are well focused overall, except in the south-west Ligurian basin (green circles: SOLA target kernels).

the magnitude of data errors, one implicitly takes into account errors inherent in the two-step nature of the inversion procedure (see Zhang et al., 2018).

3.2. Results

For SOLA–BG, we use an irregular grid in which the cell size is linearly adjusted to the raypath density at 5 s, varying from $0.1°$ to $0.8°$ (Figure 1a). SOLA targets are localized at the cell centers and their radius is given as twice the cell side. Accordingly, their size varies with the ray coverage which is an appropriate fist-order approximation for the spatial variations in resolution (Figure 1b). A Fast Marching Method (Rawlinson & Sambridge, 2005) is used jointly with SOLA–BG in order to update rays geometry and better accommodate the influence of strong velocity contrasts in the region. We calculate an optimal set of nodes (with $\alpha = 0.5$, see Section 2.2), and invert for V_s at each node using 24 parallel Markov chains performing 150,000 iterations.
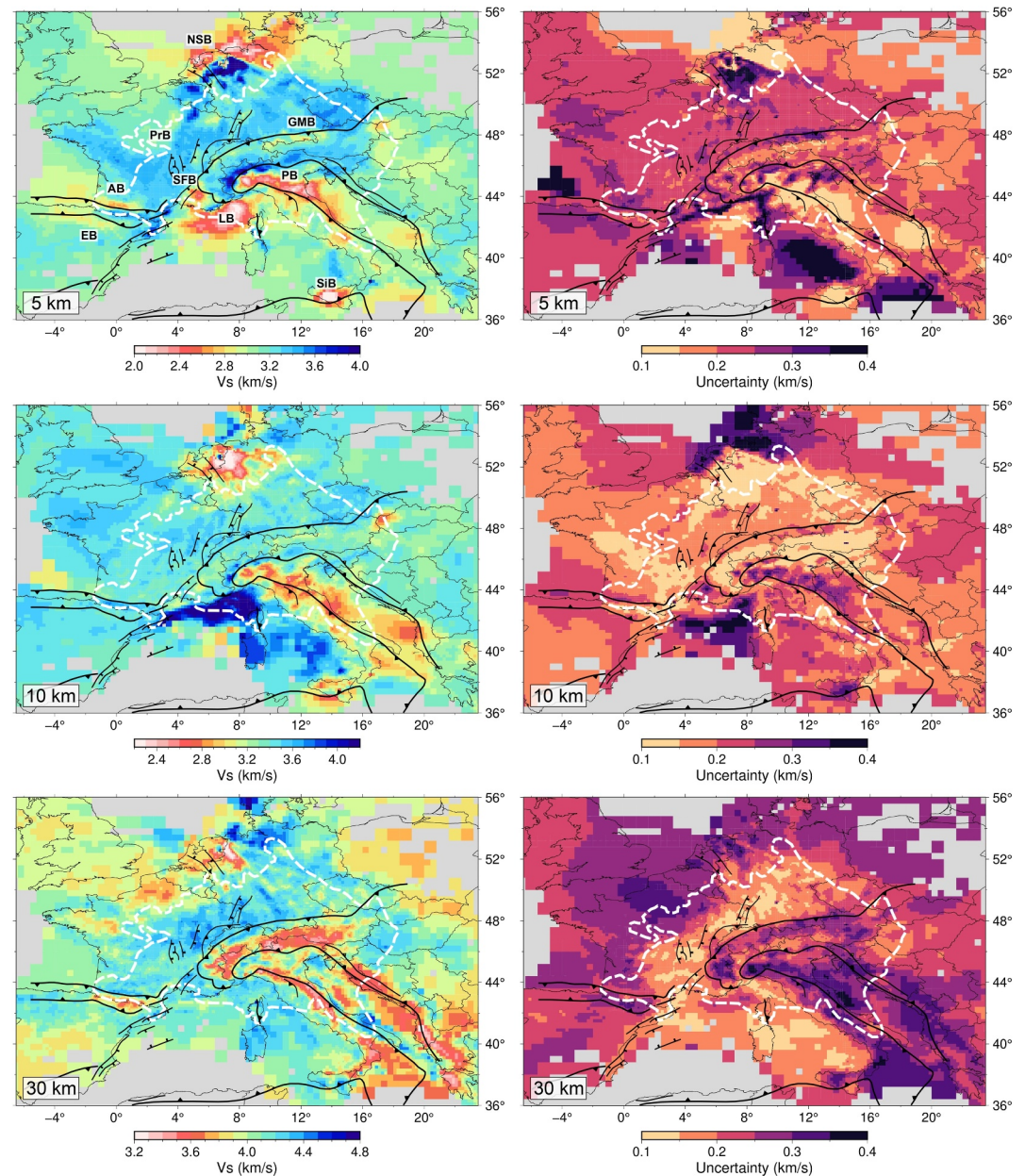
Figure 3. Depth slices in the V_s model and their uncertainty estimates given by standard deviation of the posterior ensemble of 10^5 models. The dashed white line delimits the area of resolution confidence (see Section 4.1).

Results of the tomography are summarized in Figures 2 and 3. The 5-s group velocity map and 5-km V_s depth slice display a very good correlation with surface geology (Figure 1). We clearly distinguish the main sedimentary basins, highlighted with low-velocity anomalies ($U < 2.4$ km/s, $V_s < 2.7$ km/s). The 10-km V_s slice (upper-crust) displays mantle velocities ($V_s > 4$ km/s) in the Ligurian and Adriatic basins, indicating the thinning of oceanic crust, and low velocities ($V_s = 2.9$–3 km/s) in Italy highlighting deep sediments of Po and North-Adriatic basins. The 23-s group velocity map and the 30-km V_s slice (lower-crust), exhibit low velocity anomalies along the mountain belts, reflecting the signature of deep crustal roots.

The 5-s uncertainty map exhibits low values ($\sigma < 0.035$ km/s) within some sedimentary basins, such as, Po and German Molass basins, compared to the surrounding mountain belts. We observe similar uncertainty levels along the Alps and Apennines at 23 s period (sensitive to lower-crust), while the Massif Central displays higher values ($\sigma > 0.045$ km/s). Uncertainties on the periphery of the well-covered area are relatively low ($\sigma < 0.025$ km/s), for

example, Ligurian Sea, Tyrrhenian Sea, and Northwestern France. Indeed, these regions exhibit large resolution misfit (see Figure S1 in Supporting Information S1), that is, poor, anisotropic ray coverage resulting in smeared averaging kernels, which is balanced by lower model variance. Differences of uncertainty between regions of similar averaging kernels (e.g., Alps vs. Massif Central) are likely due to variations on the quality and coherence of measurements, reflecting varying medium complexity. We can see a clear transition in the uncertainty topology toward the north-west of France; this transition marks a decrease in path density and hence an increase in the size of averaging kernels (Figure 1).

V_s uncertainty maps are given by the ensemble variance at depth. They emphasize the inversion effectiveness in explaining the dispersion curve given its uncertainty level, that is to explain the subsurface complexity. They display strong lateral variations, well correlated with the geologic structures and varying at depth (Figure 3). We observe strong uncertainty values ($\sigma > 0.3$ km/s) at 5 km depth, along the continent-ocean transitions (e.g., Ligurian-Provence and Corsican margins). Deeper, at 10 km, high uncertainties ($\sigma = 0.3$–0.4 km/s) are detected at the basis of thick sedimentary basins, for example, Ligurian and Southeast-France. In the lower crust (30 km), the south-western Alps show slightly higher uncertainties than the central and eastern Alps, which is coherent with the deep Alpine structure becoming more complex to the south-west. Overall, the French Massif central exhibits rather low uncertainties ($\sigma < 0.2$ km/s), comparable to recovered values in the oceanic domains.

Figure 2 indicates that the choice of the size of target kernels is consistent with the path density in the region. Overall, the averaging kernels are well focused within the respective SOLA targets in the well-covered areas. Nevertheless, we observe a spread of kernels located in the least covered areas (e.g., oceanic domains). This suggests the need of increasing target sizes, thereby reducing the resolution, though this effect diminishes at longer periods as the path density increases (see 23 s). Additional results are shown in Figures S4–S6 in Supporting Information S1, and a comparison with a recent ANT model is provided in Figure S7 in Supporting Information S1.

4. Discussion

4.1. Trade-off Resolution Versus Uncertainty

SOLA–BG is a powerful tool to accommodate the trade-off between resolution and uncertainty, through the explicit choice of the target kernel (T_k) (Equation 1). By fixing the targets size, we accommodated the discrepancies in raypath coverage at period. Thus, similar local resolution estimates were achieved at the cost of optimum, variable resolution over the individual periods—the size of T_k is driven by the longer periods which usually exhibit lower path density. In practice, it is impossible to achieve precisely the same local resolution, as the number, azimuthal distribution and the noise level of measurements vary between periods. One can, however, consider the query-points where the resolution-misfit reduction $\varepsilon_k = 1 - \dfrac{\sum_j \mathbb{S}_j \left(A_j^{(k)} - T_j^{(k)}\right)^2}{\sum_j \mathbb{S}_j \left(T_j^{(k)}\right)^2}$ is higher than a threshold confidence (see Figure S1 in Supporting Information S1). In our application, we considered a threshold of 65%, which corresponds to the region delimited with the dashed white line in Figure 3. One can tune this value and the size of SOLA targets to achieve a good compromise that enables reasonably precise geologic interpretations, while not degrading the resolution too much.

The SOLA trade-off is also influenced by the tunable parameter η_k which controls the propagation of uncertainties from data into the model (Equation 1). In contrast to the parameters of regularization in damped least squares (DLS) inversion methods, for example, $\|d - Gm\|^2 + \Theta^2 \|m\|^2 = \min$, where Θ is the so-called damping parameter, the choice of η_k in SOLA–BG does not induce physical misinterpretations of the velocity structures (no averaging bias, see Figure S2 in Supporting Information S1)—increasing resolution leads to higher uncertainty, and vice versa, but the solution remains "mathematically" interpretable (with respect to the "true" model). For computational reasons, we fix its value for all nodes in our application. However, one can adapt this value at each location to further fit the desired local resolution, which can be useful for small problems.

Figure 4.1 shows group velocity models of Southwestern Alps (15 s period), obtained for two different target sizes. One can see that a T_k radius of $0.2°$ is more appropriate to resolve fine velocity structures such as the so-called Ivrea body high-velocity anomaly. The recovered anomaly exhibits very good matching with the positive Bouguer anomaly (white contour in Figures 4.1c and 4.1f). Nevertheless, the $0.4°$-T_k solution better constrains the group velocities (2 times lower uncertainty values).

1. Resolution vs. Uncertainty
(SOLA-BG)
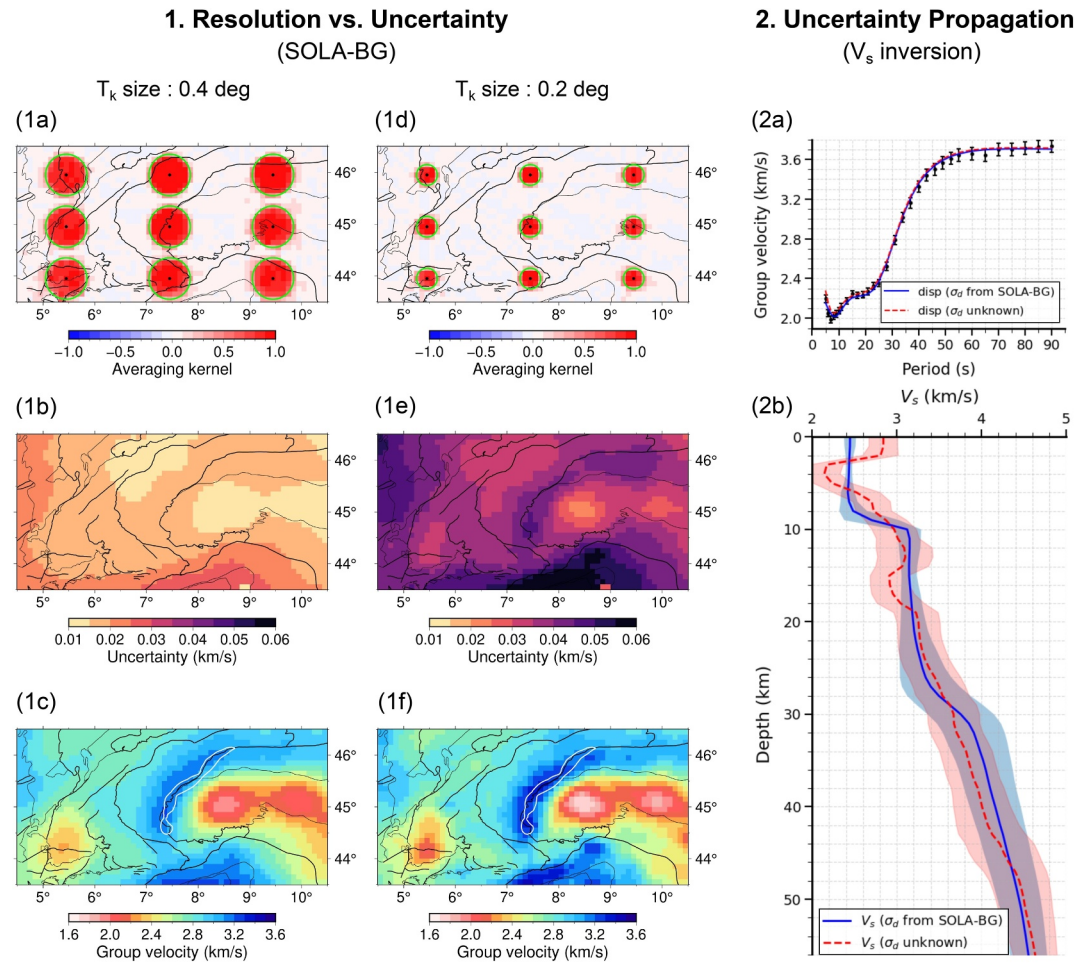
2. Uncertainty Propagation
(V_s inversion)

Figure 4. (1) SOLA–BG inversion results in the SW-Alps, using two sizes of target resolving kernels (1a–1c: 0.4°, 1d–1f: 0.2°). Green circles in 1a and 1d denote the a priori target forms. The white contour in 1c and 1f denote the so-called Ivrea body positive Bouguer anomaly (from Bigi et al., 1990). (2) Depth inversion results for a node located in Po Basin, using: (1) group velocity uncertainties from SOLA–BG (blue curves), (2) uniform uncertainty treated as unknown (red curves). Black dots and bars in 2a are SOLA–BG group velocities and their uncertainties. Note that underestimating uncertainty, when treated as unknown (prior distribution, 0.001–0.03 km/s), leads to incorrect V_s variations at depth, as a result of data over-fitting.

4.2. Computational Efficiency of the Method

4.2.1. Benefits From the Optimal Grid

Another aim of the optimal grid design (Section 2.2) is to reduce the size of the problem, hence the computational cost of the inversion at depth. In our application, the number of nodes is almost reduced by a factor of 2 (from 19,045 to 8901, see Figure S13 in Supporting Information S1). This enabled a cost reduction by a factor of 2, given that a V_s inversion on one node requires ~600 CPU seconds on a 2.7 GHz Intel platform.

It is conceptually possible to build this optimal grid prior to the 2D inversion. However, this raises the practical problem of recalculating it each time the target kernels are modified. In addition, it is better to choose a finer grid for accurate representation of the sensitivity matrix. Our choice to build this grid a posteriori is particularly relevant given that SOLA–BG is far less computationally demanding than the depth inversion (one query-point requires ~120 CPU seconds and 1 core).

4.2.2. Benefits From the Inversion Scheme

The SOLA scheme is extremely parallel since it computes the solution at each query-point independently from the others—each row of the generalized inverse is computed independently. Therefore, it adapts perfectly to the 1D character of depth inversion. This is highly useful for testing the influence of SOLA's tunable parameters on the V_s model—the dispersion curve can simply be recalculated at the considered grid node without having to recalculate the 2D group velocity maps.

4.3. Propagation of Group Velocity Uncertainties at Depth

We propagate group velocity uncertainties into V_s, by weighting the misfit of each individual period by the corresponding SOLA–BG uncertainty estimate (Equation 3). Relying on such constrained frequency-dependent estimates is a more realistic way of assessing the variance on V_s at depth. Underestimating the uncertainty level, when considered the same for all periods and treated as unknown, would limit the range of models in the solution ensemble since the inversion algorithm would over fit the dispersion curve. On the other hand, overestimating it leads to irrelevant solutions being considered as probable. The effect of a wrong choice of this parameter prior distribution is illustrated in Figure 4.2.

We considered in our application, errors in Rayleigh wave travel times increasing with the source-receiver distance, as fist-order estimate of their real magnitude. However, it is worth pointing out, even more in SOLA–BG, that a more precise evaluation of data uncertainties would further constrain the model uncertainty estimate. Our primary aim in this study was to illustrate the feasibility of our ANT approach and its efficiency in recovering self-consistent V_s models in complex geodynamic contexts. The influence of dispersion measurements uncertainties on the model appraisals will be further investigated in a future accompanied work.

5. Conclusion

We presented an innovative method for conventional ANT, based on Backus–Gilbert and Bayesian inversions. SOLA–BG yields unbiased surface wave velocities, estimated as local averages over the "true" model, and provides robust appraisals of the underlying resolution and uncertainty. We presented a method for constructing optimal depth inversion grids that adapts to the spatial variations of the local resolution at period, reducing significantly the computational cost for the 3D V_s model. We have shown that V_s can be further constrained by propagating SOLA uncertainty estimates, in the framework of Bayesian inversion. We successfully applied this ANT method at the scale of Western Europe and demonstrated its effectiveness in providing robust crustal V_s images and their appraisals, enabling meaningful quantitative interpretations.

Data Availability Statement

Seismic waveforms used in this study are publicly available from the ORFEUS Data Center (https://orfeus-eu.org/data/odc/). The "discrete" SOLA code used in this study merely consists in running the LSQR algorithm (Paige & Saunders, 1982) with specific, *study-dependent*, input matrices and vectors (e.g., data-sensitivity kernels, model-space discretization, "target" averaging kernels), as detailed in Zaroli (2016). The LSQR code is available at: https://web.stanford.edu/group/SOL/software/lsqr/ (Stanford's Systems Optimization Laboratory). Our tomographic model will be available in the ForM@Ter—EaSy Data repository (https://easydata.earth).

References

Backus, G., & Gilbert, F. (1967). Numerical applications of a formalism for geophysical inverse problems. *Geophysical Journal International*, *13*(1–3), 247–276. https://doi.org/10.1111/j.1365-246x.1967.tb02159.x

Backus, G., & Gilbert, F. (1968). The resolving power of gross Earth data. *Geophysical Journal International*, *16*(2), 169–205. https://doi.org/10.1111/j.1365-246x.1968.tb00216.x

Bensen, G., Ritzwoller, M., & Yang, Y. (2009). A 3-D shear velocity model of the crust and uppermost mantle beneath the United States from ambient seismic noise. *Geophysical Journal International*, *177*(3), 1177–1196. https://doi.org/10.1111/j.1365-246x.2009.04125.x

Bigi, G., Cosentino, D., Parotto, M., Sartori, R., & Scandone, P. (1990). Structural model of Italy and gravity map. *Quad. Ric. Sci.*, *114*.

Bodin, T., & Sambridge, M. (2009). Seismic tomography with the reversible jump algorithm. *Geophysical Journal International*, *178*(3), 1411–1436. https://doi.org/10.1111/j.1365-246x.2009.04226.x

Bodin, T., Sambridge, M., Tkalčić, H., Arroucau, P., Gallagher, K., & Rawlinson, N. (2012). Transdimensional inversion of receiver functions and surface wave dispersion. *Journal of Geophysical Research*, *117*(B2). https://doi.org/10.1029/2011jb008560

Boschi, L., & Dziewonski, A. M. (1999). High-and low-resolution images of the Earth's mantle: Implications of different approaches to tomographic modeling. *Journal of Geophysical Research*, *104*(B11), 25567–25594. https://doi.org/10.1029/1999jb900166

Chen, M., Huang, H., Yao, H., van der Hilst, R., & Niu, F. (2014). Low wave speed zones in the crust beneath SE Tibet revealed by ambient noise adjoint tomography. *Geophysical Research Letters*, *41*(2), 334–340. https://doi.org/10.1002/2013gl058476

Dziewonski, A., Bloch, S., & Landisman, M. (1969). A technique for the analysis of transient seismic signals. *Bulletin of the Seismological Society of America*, *59*(1), 427–444. https://doi.org/10.1785/bssa0590010427

Faccenna, C., Becker, T. W., Auer, L., Billi, A., Boschi, L., Brun, J. P., et al. (2014). Mantle dynamics in the Mediterranean. *Reviews of Geophysics*, *52*(3), 283–332. https://doi.org/10.1002/2013RG000444

Galetti, E., Curtis, A., Baptie, B., Jenkins, D., & Nicolson, H. (2017). Transdimensional Love-wave tomography of the British Isles and shear-velocity structure of the East Irish Sea Basin from ambient-noise interferometry. *Geophysical Journal International*, *208*(1), 36–58. https://doi.org/10.1093/gji/ggw286

Handy, M., Schmid, S., Bousquet, R., Kissling, E., & Bernoulli, D. (2010). Reconciling plate-tectonic reconstructions of Alpine Tethys with the geological-geophysical record of spreading and subduction in the Alps. *Earth-Science Reviews*, *102*(3–4), 121–158. https://doi.org/10.1016/j.earscirev.2010.06.002

Herrmann, R. B. (1973). Some aspects of band-pass filtering of surface waves. *Bulletin of the Seismological Society of America*, *63*(2), 663–671. https://doi.org/10.1785/BSSA0630020663

Hetényi, G., Molinari, I., Clinton, J., Bokelmann, G., Bondár, I., Crawford, W. C., et al. (2018). The AlpArray seismic network: A large-scale European experiment to image the alpine orogen. *Surveys in Geophysics*, *39*(5), 1009–1033. https://doi.org/10.1007/s10712-018-9472-4

Kennett, B. L., Sambridge, M. S., & Williamson, P. R. (1988). Subspace methods for large inverse problems with multiple parameter classes. *Geophysical Journal International*, *94*(2), 237–247. https://doi.org/10.1111/j.1365-246x.1988.tb05898.x

Kvapil, J., Plomerová, J., Kampfová Exnerová, H., Babuška, V., Hetényi, G., & Group, A. W. (2021). Transversely isotropic lower crust of Variscan central Europe imaged by ambient noise tomography of the Bohemian Massif. *Solid Earth*, *12*(5), 1051–1074. https://doi.org/10.5194/se-12-1051-2021

Lévêque, J.-J., Rivera, L., & Wittlinger, G. (1993). On the use of the checker-board test to assess the resolution of tomographic inversions. *Geophysical Journal International*, *115*(1), 313–318. https://doi.org/10.1111/j.1365-246x.1993.tb05605.x

Lin, F.-C., Moschetti, M. P., & Ritzwoller, M. H. (2008). Surface wave tomography of the western United States from ambient seismic noise: Rayleigh and Love wave phase velocity maps. *Geophysical Journal International*, *173*(1), 281–298. https://doi.org/10.1111/j.1365-246x.2008.03720.x

Liu, Y., Niu, F., Chen, M., & Yang, W. (2017). 3-D crustal and uppermost mantle structure beneath NE China revealed by ambient noise adjoint tomography. *Earth and Planetary Science Letters*, *461*, 20–29. https://doi.org/10.1016/j.epsl.2016.12.029

Lu, Y., Stehly, L., Paul, A., & AlpArray Working Group. (2018). High-resolution surface wave tomography of the European crust and uppermost mantle from ambient seismic noise. *Geophysical Journal International*, *214*(2), 1136–1150. https://doi.org/10.1093/gji/ggy188

Moschetti, M., Ritzwoller, M., Lin, F.-C., & Yang, Y. (2010). Crustal shear wave velocity structure of the western United States inferred from ambient seismic noise and earthquake data. *Journal of Geophysical Research*, *115*(B10). https://doi.org/10.1029/2010jb007448

Nolet, G. (2008). A breviary of seismic tomography. In *A breviary of seismic tomography*.

Nolet, G., & Montelli, R. (2005). Optimal parametrization of tomographic models. *Geophysical Journal International*, *161*(2), 365–372. https://doi.org/10.1111/j.1365-246x.2005.02596.x

Nouibat, A., Stehly, L., Paul, A., Schwartz, S., Bodin, T., Dumont, T., et al. (2022). Lithospheric transdimensional ambient-noise tomography of W-Europe: Implications for crustal-scale geometry of the W-Alps. *Geophysical Journal International*, *229*(2), 862–879. https://doi.org/10.1093/gji/ggab520

Nouibat, A., Stehly, L., Paul, A., Schwartz, S., Rolland, Y., Dumont, T., et al. (2022). Ambient-noise tomography of the Ligurian-Provence Basin using the AlpArray onshore-offshore network: Insights for the oceanic domain structure. *Journal of Geophysical Research: Solid Earth*, *127*(8), e2022JB024228. https://doi.org/10.1029/2022jb024228

Paige, C. C., & Saunders, M. A. (1982). LSQR: An algorithm for sparse linear equations and sparse least squares. *ACM Transactions on Mathematical Software*, *8*(1), 43–71. https://doi.org/10.1145/355984.355989

Paul, A., Pedersen, H. A., Bodin, T., Kästle, E., Soergel, D., Alder, C., et al. (2024). New developments in passive seismic imaging and monitoring methodological advances on seismic noise imaging in the Alpine area. *Comptes Rendus Geoscience*.

Rawlinson, N., Fichtner, A., Sambridge, M., & Young, M. K. (2014). Seismic tomography and the assessment of uncertainty. *Advances in Geophysics*, *55*, 1–76. https://doi.org/10.1016/bs.agph.2014.08.001

Rawlinson, N., & Sambridge, M. (2003). Seismic traveltime tomography of the crust and lithosphere. *Advances in Geophysics*, *46*, 81–198. https://doi.org/10.1016/s0065-2687(03)46002-0

Rawlinson, N., & Sambridge, M. (2005). The fast marching method: An effective tool for tomographic imaging and tracking multiple phases in complex layered media. *Exploration Geophysics*, *36*(4), 341–350. https://doi.org/10.1071/eg05341

Rawlinson, N., & Spakman, W. (2016). On the use of sensitivity tests in seismic tomography. *Geophysical Journal International*, *205*(2), 1221–1243. https://doi.org/10.1093/gji/ggw084

Rollet, N., Déverchère, J., Beslier, M.-O., Guennoc, P., Réhault, J.-P., Sosson, M., & Truffert, C. (2002). Back arc extension, tectonic inheritance, and volcanism in the Ligurian Sea, Western Mediterranean. *Tectonics*, *21*(3), 6-1–6-23. https://doi.org/10.1029/2001TC900027

Sadeghi-Bagerabadi, A., Vuan, A., Aoudia, A., Parolai, S. T. A., Group, A.-S.-D. W., & Tilmann, F. (2021). High-resolution crustal S-wave velocity model and Moho geometry beneath the Southeastern Alps: New insights from the SWATH-D experiment. *Frontiers in Earth Science*, *9*, 188. https://doi.org/10.3389/feart.2021.641113

Schippkus, S., Zigone, D., Bokelmann, G., & the AlpArray Working Group. (2018). Ambient-noise tomography of the wider Vienna Basin region. *Geophysical Journal International*, *215*(1), 102–117. https://doi.org/10.1093/gji/ggy259

Shapiro, N. M., Campillo, M., Stehly, L., & Ritzwoller, M. H. (2005). High-resolution surface-wave tomography from ambient seismic noise. *Science*, *307*(5715), 1615–1618. https://doi.org/10.1126/science.1108339

Stehly, L., Fry, B., Campillo, M., Shapiro, N. M., Guilbert, J., Boschi, L., & Giardini, D. (2009). Tomography of the Alpine region from observations of seismic ambient noise. *Geophysical Journal International*, *178*(1), 338–350. https://doi.org/10.1111/j.1365-246x.2009.04132.x

Sun, X., Song, X., Zheng, S., Yang, Y., & Ritzwoller, M. H. (2010). Three dimensional shear wave velocity structure of the crust and upper mantle beneath China from ambient noise surface wave tomography. *Earthquake Science*, *23*(5), 449–463. https://doi.org/10.1007/s11589-010-0744-4

Trampert, J., Fichtner, A., & Ritsema, J. (2013). Resolution tests revisited: The power of random numbers. *Geophysical Journal International*, *192*(2), 676–680. https://doi.org/10.1093/gji/ggs057

Wang, K., Yang, Y., Basini, P., Tong, P., Tape, C., & Liu, Q. (2018). Refined crustal and uppermost mantle structure of southern California by ambient noise adjoint tomography. *Geophysical Journal International*, *215*(2), 844–863. https://doi.org/10.1093/gji/ggy312

Yuan, H., & Bodin, T. (2018). A probabilistic shear wave velocity model of the crust in the central West Australian craton constrained by transdimensional inversion of ambient noise dispersion. *Tectonics*, *37*(7), 1994–2012. https://doi.org/10.1029/2017tc004834

Zaroli, C. (2010). Global multiple-frequency S-wave tomography of the Earth's mantle (Unpublished doctoral dissertation).

Zaroli, C. (2016). Global seismic tomography using Backus–Gilbert inversion. *Geophysical Journal International*, *207*(2), 876–888. https://doi.org/10.1093/gji/ggw315

Zaroli, C., Koelemeijer, P., & Lambotte, S. (2017). Toward seeing the Earth's interior through unbiased tomographic lenses. *Geophysical Research Letters*, *44*(22), 11–399. https://doi.org/10.1002/2017gl074996

Zhang, X., Curtis, A., Galetti, E., & De Ridder, S. (2018). 3-D Monte Carlo surface wave tomography. *Geophysical Journal International*, *215*(3), 1644–1658. https://doi.org/10.1093/gji/ggy362

Zheng, Y., Shen, W., Zhou, L., Yang, Y., Xie, Z., & Ritzwoller, M. H. (2011). Crust and uppermost mantle beneath the North China Craton, northeastern China, and the Sea of Japan from ambient noise tomography. *Journal of Geophysical Research*, *116*(B12), B12312. https://doi.org/10.1029/2011jb008637